Reaction Kinetics, Mechanisms and Catalysis (2021) 134:1003–1015
https://doi.org/10.1007/s11144-021-02107-4

Preparation of a zinc-based metal–organic framework (MOF-5)/BiOBr heterojunction for photodegradation of Rhodamine B

Anna Chen[1] · Jin Zhang[1] · Yi Zhou[1] · Haiqin Tang[1]

Received: 20 August 2021 / Accepted: 29 October 2021 / Published online: 15 November 2021

Abstract

In this study, the MOF-5/BiOBr photocatalyst with microsphere structure was synthesized by hydrothermal method for the first time. The crystal structure, morphology, photoelectric performance and photocatalytic activity of the samples were characterized by XRD, SEM, TEM, XPS and electrochemistry. The results show that the synthesized MOF-5/BiOBr photocatalyst exhibits better photocatalytic performance than pure MOF-5 and BiOBr under simulated sunlight. The efficiency of Rhodamine B (RhB) removal based MOF-5/BiOBr composite (MOF-5 with mass ratio of MOF-5/BiOBr = 20 wt% of) reached 99.7%. The possible photocatalytic mechanism is discussed through the capture experiment of active species. The enhanced photocatalytic performance of the MOF-5/BiOBr composite may be related to the interaction between BiOBr and MOF-5 and the type II charge transfer path. The catalyst has simple preparation process, low cost, high activity under natural light, and high efficiency, and is expected to play a role in the treatment of environmental wastewater. This work provides a new insight for designing MOF-5 based photocatalyst.

Keywords MOF-5 · BiOBr · Type II heterojunction · Photocatalytic

Introduction

With the development of industry, water pollution caused by antibiotics, heavy metals, and industrial dyes has become more and more serious [1–4]. At present, there are various technologies and strategies to selectively remove or purify pollutants, including adsorption [5], advanced oxidation [6], microwave catalysis [7] and photocatalysis [8, 9].Photocatalysis is an environmentally friendly and efficient method due to its mild conditions, high catalytic efficiency and simple experimental

✉ Jin Zhang
jinzhang@csust.edu.cn

[1] School of Chemistry and Chemical Engineering, Changsha University of Science and Technology, Changsha 410000, China

operation [10–13]. However, the limited solar energy absorption range and low quantum efficiency of photocatalyst, hinder its wider application in actual wastewater treatment [14–17]. Therefore, it is necessary to further explore more effective and higher catalytic activity of visible light reaction semiconductor photocatalytic materials.

BiOBr is an indirect semiconductor with special layered structure and a high degree of anisotropy, which exhibits great potential applications in photocatalytic degradation, carbon dioxide reduction, nitrogen fixation and hydrogen evolution [18–22]. BiOBr exhibits excellent photoelectric properties due to its special layered structure that can form an internal electric field. The BiOBr has a band gap of about 2.6 eV and two unique valence bands that show different oxidation capacities: one responds to visible light and the other to ultraviolet light [23, 24]. However, the conversion efficiency of BiOBr to solar energy is still limited by several shortcomings, such as inappropriate band structure, large band gap and unsatisfactory particle size, etc. [25, 26]. Various approaches have been adopted to address these limitations, including crystal face exposure, loading of precious metal particles, construction of heterojunctions, and composite modification. Sun et al. [27] synthesized BiOBr catalysts with different microstructure by adjusting solvothermal conditions. The result showed that the exposed BiOBr (110) crystal plane can obtain more oxygen defects. The BiOBr microflowers exhibited good photocatalytic degradation of gaseous o-dichlorobenzene under visible light. Jia et al. [28] prepared BiOBr/$BiOAc_{1-x}Br_x$ S-scheme heterojunction photocatalyst. When the molar ratio of Br/Bi was 0.8, it showed good visible light catalysis for the degradation of tetracycline (TC) and Rhodamine B (RhB), with degradation efficiency of 99.2% and 99.4%. Wang et al. [29] synthesized a size-matched Sb_2WO_6/BiOBr photocatalyst using a precipitation-deposition method for the removal of NO.

Metal–organic frameworks (MOFs) have been widely used in various technical and scientific fields due to their controllable pore capacity and large specific surface area. Some representative MOFs (such as ZIF-8 [30], MOF-5 [31], MIL-125 [32], MIL-53 [33], MIL-101 [34] and UiO-66 [35]) have potential application value. MOF-5 has a cubic topology, which is formed by organic ligands and metal zinc ions in a specific conjugate structure [36–38]. This structure can promote charge transport and help reduce photo-generated electron–hole recombination [31, 39]. However, MOF-5 is easily hydrolyzed when the water content reaches 4% [40], and a large number of studies focused on how to explore a waterproof framework while ignoring the potential application of hydrolyzed MOF-5. Among them, Jeong et al. found that the effect of hydrolyzed MOF-5 can be eliminated in the heat treatment process [41].

As a widely used nitrogenous dye pollutant, RhB belongs to three types of carcinogens. Conventional wastewater treatment methods such as biological oxidation cannot effectively remove aromatic amines in wastewater, and may even produce potentially carcinogenic aromatic amines [42]. Therefore, this article uses the hydrothermal method to load MOF-5 on the BiOBr surface to form a scheme II heterojunction MOF-5/BiOBr system. The photocatalytic performance of MOF-5/BiOBr was evaluated by dissociating RhB in simulated solar degradation. A possible scheme II photocatalytic degradation mechanism was proposed by XPS and UV–Vis

diffuse reflectance spectroscopy, free radical capture experiment, and Mott–Schottky results to explore the photocatalytic degradation mechanism.

Experimental

Reagent

Cetyltrimethylammonium bromide (CTAB), terephthalic acid ($C_8H_6O_4$), and absolute ethanol were purchased from Sinopharm Chemical Reagent Co., Ltd. Rhodamine B (RhB) and bismuth nitrate pentahydrate ($Bi(NO_3)_3{\cdot}5H_2O$) were purchased from Aladdin Industries. Zinc acetate dihydrate ($Zn(CH_3CO_2)_2{\cdot}2H_2O$) was purchased from Tianjin Guangxia Technology Development Co., Ltd. All reagents are analytically pure and no further purification is required. Deionized water was used throughout the experiment.

Preparation of MOF-5

Terephthalic acid was dissolved in 60 mL of DMF, followed by $Zn(CH_3CO_2)_2{\cdot}2H_2O$ added to the solution and stirred well [43]. The mixture was transferred into a 100 mL Teflon-lined autoclave and kept at 100 ℃ for 12 h. After the Teflon-lined autoclave was cooled to room temperature, the collected products were washed three times with DMF, dried at 60 °C for 6 h, and samples were collected.

Preparation of MOF-5/BiOBr

Weighed 0.7282 g CTAB was dissolved in 20 mL ethanol as solution a. 0.9701 g $Bi(NO_3)_3{\cdot}5H_2O$ and a predetermined amount of MOF-5 were dissolved in 20 mL ethanol as solution b. Under vigorous stirring, add solution a to solution b for 1 h to form a homogeneous solution. The mixture was transferred to a 100 mL Teflon-lined autoclave and kept at 160 °C for 16 h. The product was washed three times with ethanol and water. The samples were collected by drying at 60 °C for several hours. MOF-5/BiOBr composite material represents X%MB (X% represents the mass ratio of MOF-5 to BiOBr, X is 10, 15, 20, 25, 30).

The method of synthesis of pure BiOBr is the same as that of MOF-5/BiOBr except that MOF-5 is not added.

Characterization

Scanning electron microscope (SEM, Zeiss Sigma300) and field emission transmission electron microscope (FE-TEM, Tecnai G2 F20) were used to test the microstructure and morphology of the samples. Using the Brucker D8 phase X-ray diffractometer (XRD) to measure the crystal structure of the sample. A Thermo Scientific K-Alpha X-ray Photoelectron Spectrometer (XPS) was used to obtain the element composition and valence state of the sample. UV–Vis diffusion spectroscopy

(UV-2600 Lambda750 PE) was used to test the light absorption characteristics of the prepared samples at a wavelength of 200–800 nm. The specific surface area and porosity analyzer of Mike's model 2020 HD88 was used to test the samples.

Photocatalytic performance test

In order to evaluate the photocatalytic activity of synthetic materials, the degradation efficiency of RhB was tested. A sample of 10 mg was weighed and added into 100 mL of RhB solution with a concentration of 10 ppm, sonicate for 5 min, and magnetically stir the suspension in a dark environment for 1 h to establish an adsorption–desorption equilibrium. Then, under simulated sunlight, 4 mL of the suspension was taken every 3 min. The 4 mL suspension was centrifuged at a high speed to precipitate and separate the photocatalyst, and the supernatant was obtained. The absorbance of the supernatant was measured at 554 nm using a 721 visible spectrophotometer. The photocatalytic degradation of each sample follows the non-linear least squares fitting equation:

$$A = X * ecp\left(-k_{app} * t\right) + E, \tag{1}$$

A is the amplitude of the process, X is the concentration of reactant after degradation of RhB, E is the end point, and k_{app} is the degradation rate constant.

Electrochemical test

The electrochemical impedance spectra and Mott–Schottky curves of the materials were measured using a three-electrode cell system at the Electrochemical Workstation (Model CHI660C) in Chenhua, Shanghai. BiOBr and MOF-5 (effective area 1 cm^2) prepared on FTO conductive glass are used as working electrodes. The electrolyte is 0.5 mol/L sodium sulfate solution.

Results and discussion

The crystal structure of the sample was characterized by X-ray diffraction technique. As shown in Fig. 1, the main diffraction peaks of pure BiOBr are located at $2\theta = 10.9°$, 25.2°, 32.2°, 46.2°, and 56.7°, which are consistent with the standard spectrum of tetragonal BiOBr (JCPDS No. 09-0393) and correspond to the crystal planes (001), (101), (110), (200) and (212). The characteristic peaks of sample MOF-5 at $2\theta = 6.77°$, 9.70°, 13.71°, and 15.56° correspond to (200), (220), (400) and (420) crystal planes, which are consistent with previous literature reports [43]. Compared with that of pure BiOBr, the diffraction peak of MOF-5/BiOBr composite material, with the increase of MOF-5, the peak intensity of 2θ about 12.5° becomes more and more obvious. The results showed that the MOF-5 and BiOBr composite materials were successfully prepared.

The morphology of the sample was characterized by scanning electron microscope. As shown in Fig. S1a, the width of the MOF-5 cubic crystal is about 2 μm.

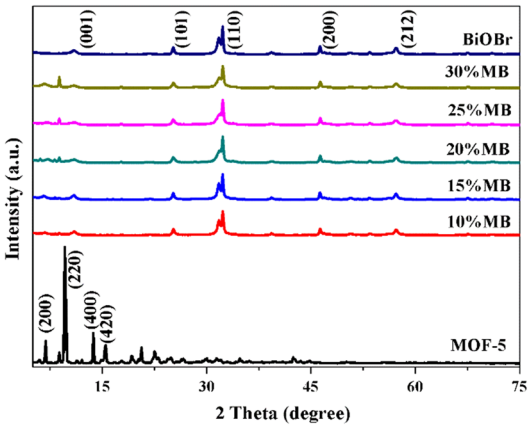

Fig. 1 X-ray diffractometer pattern of MOF-5, 10%MB, 15%MB, 20%MB, 25%MB, 30%MB and BiOBr(XRD condition: Bruker D8 Advance, 5°–90°, 10°/min)

As shown in Fig. S1b, BiOBr is self-assembled from nanosheets into microspheres of approximately 3 μm. Fig. S1c is the SEM image of the 20% MB composite. It can be seen from the figure that the structure of MOF-5 has undergone significant changes, and the cubic crystals have been transformed into needle-shaped nanosheets [36–38], which are loaded on the surface of BiOBr. In addition, energy dispersive X-ray (EDX) mapping was performed on the element distribution of the 20% MB sample. The distribution diagrams of Bi, O, Br, and Zn elements are shown in the Fig. S1. SEM shows that the composite has been successfully prepared, which is consistent with the XRD results.

TEM and high resolution TEM (HRTEM) are used to further prove that MOF-5 is supported on BiOBr. As shown in the figure, the TEM image in Fig. S2 is 20%MB, which shows that it is composed of sheet structure. Compared with the SEM image, the sheet is more dispersed, which is due to the selection of more broken areas. Fig. S2b depicts an HRTEM image of 20% MB, a lattice fringe spacing of 0.277 nm, corresponding to the crystal plane of the tetragonal BiOBr (110), confirming the XRD results. Since MOF-5 has no lattice stripes, the blank space is MOF-5. MOF-5 was grown on BiOBr nanosheets, indicating that there is an interface contact between the two semiconductors, which is conducive to the separation of photogenerated carriers.

The valence state, surface composition and chemical state of the sample were analyzed by XPS spectroscopy. As shown in Fig. 2, the O 1s of BiOBr is on two peaks around 532.17 eV and 530.08 eV, which are attributed to the BiOBr and the oxygen species adsorbed on the Bi-O bond surface of the sample, such as hydroxyl or H_2O. With the increase of MOF-5 loading, the binding energy decreased, and the lattice oxygen peak of 20% MB shifted to 529.99 eV. The two peaks at 69.65 eV (Br $3d_{3/2}$) and 68.47 eV (Br $3d_{5/2}$) are assigned to the spin–orbit splitting of Br 3d, indicating the presence of Br^- anions (Fig. 2b). In the XPS spectrum of Bi 4f (Fig. 2c), the observed binding energy peaks are around 164.59 eV (Bi $4f_{5/2}$) and 159.29 eV (Bi $4f_{7/2}$), confirming that the bismuth species in the product is Bi^{3+}. On Fig. 2d, Zn $2p_{3/2}$ was observed at 1021.91 eV and 1044.93 eV, indicating the presence of BDC

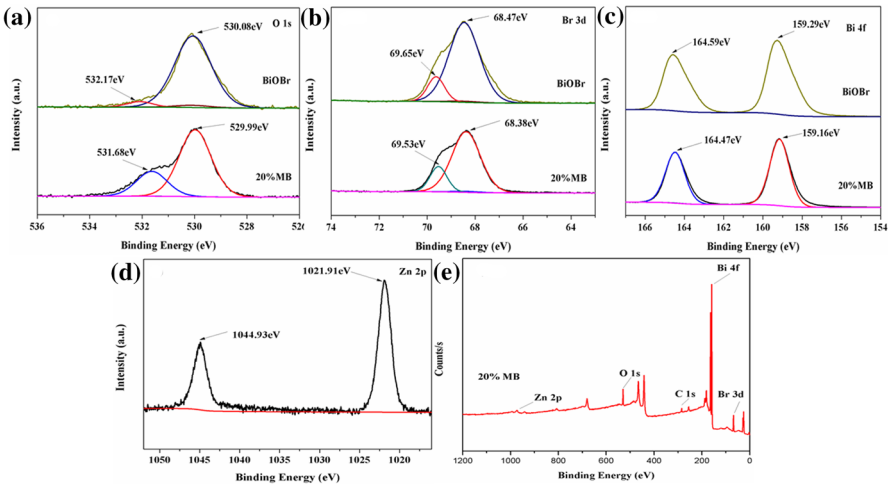

Fig. 2 X-ray photoelectron spectroscopy (XPS) spectra of pure BiOBr and 20% MB

ligand complexes, which are consistent with the framework group of zinc carboxylate. Compared with BiOBr, the binding energies of O 1s, Bi 4f and Br 4d at 20% MB peak position decreased. The negative shift of binding energy shows an increase in BiOBr electron density, indicating that the surface binding interaction between MOF-5 and BiOBr and the charge transfer from the surface of MOF-5 to BiOBr. The changes in binding energies Bi 4f, Br 4d and O 1s indicate that the chemical environment of Bi 4f, Br 4d and O 1s has changed. The surface electron density caused by the change in charge redistribution can be attributed to the MOF-5 load. Also, Fig. 2e shows the survey spectra of XPS with 20% MB. By semi-quantitative analysis of the elements in the XPS spectrum, the elemental ratios of Bi/Zn, O/Zn, Br/Zn can be obtained: 19.71:3.09; 26.91:3.09; 13.19:3.09. It is consistent with the result of EDS in SEM, It further confirmed the successful preparation of MOF-5 and BiOBr.

As shown in the Fig. 3, the specific surface area and BJH pore structure of the samples BiOBr, MOF-5 and 20%MB composite materials were studied. According to the IUPAC classification, the isotherms of BiOBr, MOF-5 and 20% MB correspond to the type IV and type H3 hysteresis loop, indicating the existence of mesopores and the material recombination has almost no effect on the adsorption capacity of the sample. In addition, the BET specific surface areas of MOF-5, BiOBr and 20%MB are 3.7763 m^2/g, 16.9192 m^2/g and 16.1288 m^2/g. Compared with the BiOBr, the BET specific surface area of 20% MB is slightly reduced, but higher than that of MOF-5, indicating that the specific surface area of the composite is not the main factor affecting the photocatalytic activity [44, 45] (Table 1).

Tested the ultraviolet–visible diffuse reflectance spectrum (UV–Vis DRS), as shown in the Fig. 4. Obviously, the light absorption edge of BiOBr is 440 nm, which indicates that BiOBr microspheres have partial absorption in the visible light region. However, MOF-5 shows obvious light absorption in the ultraviolet region. It can be

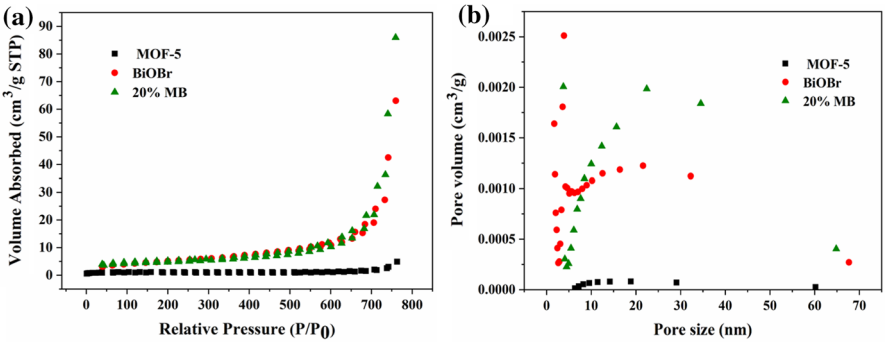

Fig. 3 MOF-5, BiOBr, 20% MB: **a** N_2 adsorption–desorption isotherm; **b** BJH pore size distribution diagram

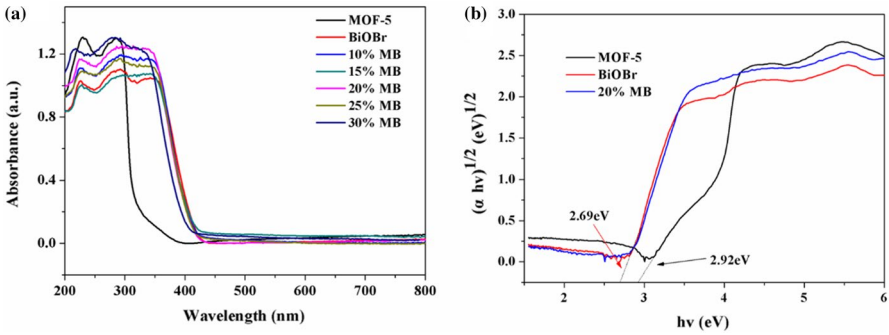

Fig. 4 **a** Ultraviolet–visible diffuse reflectance spectra of MOF-5, BiOBr and composite materials; **b** band gap distribution of BiOBr, MOF-5 and 20% MB (UV–Vis diffusion spectroscopy condition: UV-2600 Lambda 750 PE, Wavelength range: 200–800 nm, Absorption ratio reference: $BaSO_4$; Eg calculation formula: $[\alpha h\nu)^n = A(h\nu - E_g)]$

seen from Fig. 4a that compared with BiOBr, 20% MB has only a slight red shift. The reason for the red shift may be attributed to the interaction of the heterojunction formed by MOF-5 and BiOBr. According to the reflectance data, the E_g of the sample is further estimated by the formula:

$$(\alpha h\nu)^n = A\left(h\nu - E_g\right), \tag{2}$$

The E_g of BiOBr, MOF-5 and 20%MB are 2.69 eV, 2.92 eV, and 2.62 eV.

The photocatalytic activity of the prepared samples was evaluated by simulating the degradation of RhB under sunlight irradiation. Fig. 3a is a graph showing the degradation of RhB by pure BiOBr and MB composites under xenon lamp irradiation for 18 min. It can be seen from the figure that the MB materials loaded with different masses of MOF-5 show different photocatalytic degradation activities, and the order was 20%MB > 25%MB > 15%MB > 30%MB > 10%MB > BiOBr > MOF-5, the degradation rates were 99.7%, 98.4%, 95.5%, 93.8%, 89.4%, 76.6% and 2.1%.

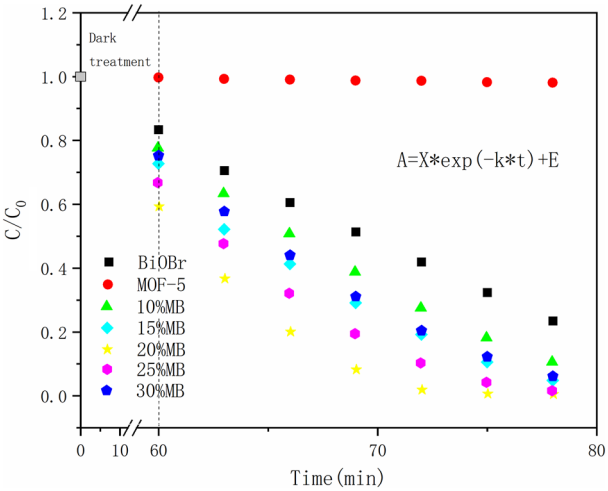

Fig. 5 Photocatalytic degradation of RhB by MOF-5, BiOBr, 10%MB, 15%MB, 20%MB, 25%MB and 30%MB (experimental conditions: $[RhB]_0 = 10$ mg/L, [Catalyst = 10 mg], $V_{solution} = 100$ ml, $\lambda > 420$ nm, irradiation time: 18 min, nonlinear least square fits-lines)

Table 1 BET specific surface area, pore size and pore volume of BiOBr, MOF-5 and 20% MB

Sample	BET surface area (m^2/g)	Pore volume (cm^3/g)	Pore Size (nm)
BiOBr	16.9192	0.097850	21.3334
MOF-5	3.7763	0.006408	30.1215
20%MB	16.1288	0.132903	27.8799

Table 2 The standard deviation (σ) for photocatalytic degradation RhB with correlation coefficient value (R^2) a and the rate constants by the non-linear least squares fitting

Sample	kapp*(min^{-1})	σ	R^2
BiOBr	0.018	0.006	0.9988
MOF-5	0.015	0.024	0.9764
10%MB	0.036	0.003	0.9996
15%MB	0.067	0.01	0.9966
20%MB	0.164	0.02	0.9916
30%MB	0.098	0.009	0.9977
25%MB	0.061	0.004	0.9994

The entire photocatalytic degradation process conforms to non-linear least squares ftting equation. The rate constant, standard deviation (σ) and correlation coefficient value (R^2) of 20% MB, 25% MB, 15% MB, 30% MB, 10% MB, BiOBr and MOF-5 (Table 2) are shown in Table 2. Obviously, the 20% MB composite has the highest rate constant.

The function of free radicals in the photodegradation process was measured by the active substance capture experiment (Fig. S3), and p-benzoquinone (BQ, 5.0 mg), triethanolamine (TEOA, 0.1 mL) and isopropanol (IPA, 0.4 mL) were selected as a capture agent for capture experiments. When TEOA and BQ were added to the photocatalytic system, the degradation of RhB by 20% MB was negligible, and the photocatalytic activity was completely inhibited. The results show that h^+ and $\cdot O_2^-$ play important roles in photocatalytic reactions. When IPA was added to the photocatalytic system, the degradation of RhB did not change, indicating that ·OH had no effect in the degradation process. In order to evaluate the stability of the prepared photocatalyst, the RhB degradation experiment of the 20% MB composite was repeated under the same conditions. As shown in Fig. S4, after four cycles of experiments, the photocatalytic activity of the 20% MB composite material showed only a slight change (1.3%), indicating that the prepared 20% MB composite material has good photocatalytic stability.

The electrochemical impedance (EIS) experiment is used to analyze the photoelectric properties of the material. As shown in the Fig. S5, compared with the monomer, the radius of the impedance semicircle on the 20%MB Nyquist diagram is the smallest, the electron transfer process is faster, and the electron transfer resistance on the surface of the composite material is lower. According to the above results, the photoelectric performance of 20% MB is more effective than pure BiOBr (Fig. 6).

The flat band potentials of BiOBr and MOF-5 can be obtained by Mott–Schottky diagram.

$$\frac{1}{C^2} = \frac{2}{A^2 e \varepsilon \varepsilon_0 N_A}\left(E - E_{FB} - \frac{kT}{V}\right), \tag{3}$$

Through the Mott–Schottky curve, the EFB value can be obtained. The slope of the tangent line is positive, indicating that the pure BiOBr and MOF-5 have n-type semiconductor characteristics. It is generally believed that for n-type semiconductors, the flat band potential is positive 0.2 V than the conduction band

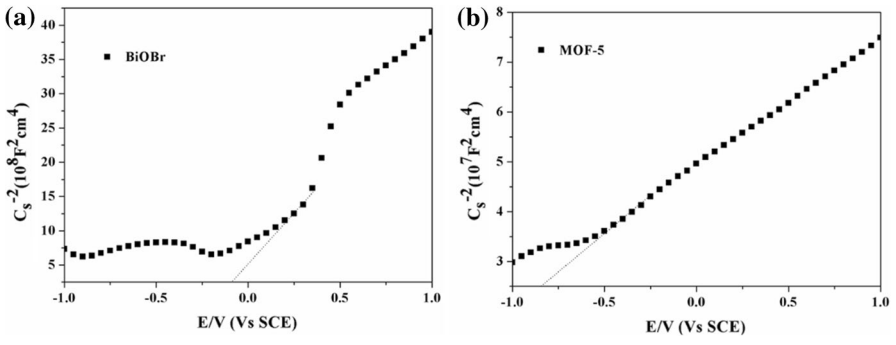

Fig. 6 Mott–Schottky diagram of **a** BiOBr and **b** MOF-5(M-S diagram condition: Model CHI660C, 0.5 mol/L sodium sulfate solution, − 1.0 to 1.0 V)

potential. The calculated conduction band potentials of BiOBr and MOF-5 are − 0.28 V and − 1.04 V.

Photocatalytic mechanism

Through UV–Visible diffuse reflectance spectroscopy and Mott–Schottky calculations, the conduction band (CB) potential and valence band (VB) potential of BiOBr are − 0.28 V and 2.41 V, respectively, and the conduction band (CB) potential and valence band (VB) potentials of MOF-5 are − 1.04 V and 1.88 V, respectively. As shown in the figure, under simulated sunlight, both BiOBr and MOF-5 can be excited to obtain photo-generated electron–hole pairs. Since the CB value (− 0.28 V) of BiOBr is more corrected than the standard redox potential (− 0.33 V vs. NHE) of $\cdot O_2/\cdot O_2^-$, the accumulated electrons on the CB of BiOBr cannot have a high enough reduction potential to form $\cdot O_2/\cdot O_2^-$. At the same time, because the VB value of MOF-5 (1.88 V) is more negative than the potential of $H_2O/\cdot OH$ (1.99 V vs NHE), the holes on the VB of MOF-5 can hardly generate $H_2O/\cdot OH$ radicals. By XPS test, the charge was found to migrate from the MOF-5 surface to BiOBr. Therefore, the photocatalytic reaction mechanism belongs to type II heterojunction.

BiOBr and MOF-5 act as an oxidation photocatalyst with a lower Fermi level and a reducing semiconductor with a higher Fermi level. After BiOBr and MOF-5 contact with each other and form a heterojunction, the charge is transferred from MOF-5 to BiOBr until the Fermi level reaches equilibrium. Under the irradiation of light, the photogenerated electrons in the CB of BiOBr will migrate to the VB of MOF-5 through the intimate interface, and recombine with holes under the driving force of the product. In the field of electronics, both useful electrons and holes with higher redox potential are retained on the CB of MOF-5 and the VB of BiOBr. Moreover, RhB is excited by light to produce e^- and RhB*. Since the LUMO of RhB is − 1.04 eV, which is lower than the CB of MOF-5 and BiOBr, the e^- generated by RhB excited by light can migrate to the CB of MOF-5 and BiOBr. This is the dye sensitization effect of RhB [46, 47]. As a result, the electrons on the CB of MOF-5 can react with $\cdot O_2$ to form $\cdot O_2^-$, and the holes on the VB of BiOBr can oxidize H_2O to ·OH. Subsequently, these active substances will decompose pollutants.

Conclusion

In summary, a series of type II heterojunction MOF-5/BiOBr composites were prepared by hydrothermal method. Compared with the monomer BiOBr, the degradation rate of RhB by 20wt%MB composite material increased by 4 times within 18 min after xenon lamp irradiation. This catalyst is expected to play an important role in the treatment of environmental wastewater. In addition, the microstructure of the heterojunction with high dispersibility can provide more reaction sites. This work provides enlightenment for the design of high-efficiency heterojunction photocatalysts using a simple synthesis route.

Supplementary Information The online version contains supplementary material available at https://doi.org/10.1007/s11144-021-02107-4.

Acknowledgements This work was supported by Hunan Collaborative Innovation Center of Environmental and Energy Photocatalysis and the National Natural Science Foundation of China (No. 21671026).

Declarations

Conflict of interest The authors declare no conflict of interest.

References

1. Pirhashemi M, Habibi-Yangjeh A, Rahim Pouran S (2018) Review on the criteria anticipated for the fabrication of highly efficient ZnO-based visible-light-driven photocatalysts. J Ind Eng Chem 62:1–25. https://doi.org/10.1016/j.jiec.2018.01.012
2. Shekofteh-Gohari M, Habibi-Yangjeh A, Abitorabi M, Rouhi A (2018) Magnetically separable nanocomposites based on ZnO and their applications in photocatalytic processes: a review. Crit Rev Environ Sci Technol 48:806–857. https://doi.org/10.1080/10643389.2018.1487227
3. Akhundi A, Habibi-Yangjeh A, Abitorabi M, Rahim Pouran S (2019) Review on photocatalytic conversion of carbon dioxide to value-added compounds and renewable fuels by graphitic carbon nitride-based photocatalysts. Catal Rev 61:595–628. https://doi.org/10.1080/01614940.2019.1654224
4. Zhang J, Yuan X, Si M, Jiang L, Yu H (2020) Core-shell structured cadmium sulfide nanocomposites for solar energy utilization. Adv Colloid Interface Sci 282:102209. https://doi.org/10.1016/j.cis.2020.102209
5. Liu D, Huang Z, Li M, Li X, Sun P, Zhou L (2020) Construction of magnetic bifunctional beta-cyclodextrin nanocomposites for adsorption and degradation of persistent organic pollutants. Carbohydr Polym 230:115564. https://doi.org/10.1016/j.carbpol.2019.115564
6. Camargo-Perea AL, Rubio-Clemente A, Peñuela GA (2020) Use of ultrasound as an advanced oxidation process for the degradation of emerging pollutants in water. Water. https://doi.org/10.3390/w12041068
7. Ling L, Feng Y, Li H, Chen Y, Wen J, Zhu J, Bian Z (2019) Microwave induced surface enhanced pollutant adsorption and photocatalytic degradation on Ag/TiO_2. Appl Surf Sci 483:772–778. https://doi.org/10.1016/j.apsusc.2019.04.039
8. An W, Tian L, Hu J, Liu L, Cui W, Liang Y (2020) Efficient degradation of organic pollutants by catalytic ozonation and photocatalysis synergy system using double-functional MgO/g-C_3N_4 catalyst. Appl Surf Sci. https://doi.org/10.1016/j.apsusc.2020.147518
9. Zhang J, Yuan X, Jiang L, Wu Z, Chen X, Wang H, Wang H, Zeng G (2018) Highly efficient photocatalysis toward tetracycline of nitrogen doped carbon quantum dots sensitized bismuth tungstate based on interfacial charge transfer. J Colloid Interface Sci 511:296–306. https://doi.org/10.1016/j.jcis.2017.09.083
10. Wang Y, He J, Zhu Y, Zhang H, Yang C, Wang K, Wu S-c, Chueh Y-L, Jiang W (2020) Hierarchical Bi-doped BiOBr microspheres assembled from nanosheets with (0 0 1) facet exposed via crystal facet engineering toward highly efficient visible light photocatalysis. Appl Surf Sci. https://doi.org/10.1016/j.apsusc.2020.145927
11. Wang K, Zhang Y, Liu L, Lu N, Zhang Z (2019) BiOBr nanosheets-decorated TiO_2 nanofibers as hierarchical p–n heterojunctions photocatalysts for pollutant degradation. J Mater Sci 54:8426–8435. https://doi.org/10.1007/s10853-019-03466-z
12. Zhang J, Yan M, Yuan X, Si M, Jiang L, Wu Z, Wang H, Zeng G (2018) Nitrogen doped carbon quantum dots mediated silver phosphate/bismuth vanadate Z-scheme photocatalyst for enhanced antibiotic degradation. J Colloid Interface Sci 529:11–22. https://doi.org/10.1016/j.jcis.2018.05.109
13. Si M, Zhang J, He Y, Yang Z, Yan X, Liu M, Zhuo S, Wang S, Min X, Gao C, Chai L, Shi Y (2018) Synchronous and rapid preparation of lignin nanoparticles and carbon quantum dots from natural lignocellulose. Green Chem 20:3414–3419. https://doi.org/10.1039/c8gc00744f

14. Sheng Y, Wei Z, Miao H, Yao W, Li H, Zhu Y (2019) Enhanced organic pollutant photodegradation via adsorption/photocatalysis synergy using a 3D g-C_3N_4/TiO_2 free-separation photocatalyst. Chem Eng J 370:287–294. https://doi.org/10.1016/j.cej.2019.03.197
15. Ai Z, Shao Y, Chang B, Zhang L, Shen J, Wu Y, Huang B, Hao X (2019) Rational modulation of p-n homojunction in P-doped g-C_3N_4 decorated with Ti_3C_2 for photocatalytic overall water splitting. Appl Catal B. https://doi.org/10.1016/j.apcatb.2019.118077
16. Yuan X, Zhang J, Yan M, Si M, Jiang L, Li Y, Yu H, Zhang J, Zeng G (2019) Nitrogen doped carbon quantum dots promoted the construction of Z-scheme system with enhanced molecular oxygen activation ability. J Colloid Interface Sci 541:123–132. https://doi.org/10.1016/j.jcis.2019.01.072
17. Zhang J, Si M, Jiang L, Yuan X, Yu H, Wu Z, Li Y, Guo J (2021) Core-shell Ag@nitrogen-doped carbon quantum dots modified $BiVO_4$ nanosheets with enhanced photocatalytic performance under Vis-NIR light: synergism of molecular oxygen activation and surface plasmon resonance. Chem Eng J. https://doi.org/10.1016/j.cej.2020.128336
18. Li R, Liu J, Zhang X, Wang Y, Wang Y, Zhang C, Zhang X, Fan C (2018) Iodide-modified $Bi_4O_5Br_2$ photocatalyst with tunable conduction band position for efficient visible-light decontamination of pollutants. Chem Eng J 339:42–50. https://doi.org/10.1016/j.cej.2018.01.109
19. Rashid J, Abbas A, Chang LC, Iqbal A, Haq IU, Rehman A, Awan SU, Arshad M, Rafique M, Barakat MA (2019) Butterfly cluster like lamellar BiOBr/TiO_2 nanocomposite for enhanced sunlight photocatalytic mineralization of aqueous ciprofloxacin. Sci Total Environ 665:668–677. https://doi.org/10.1016/j.scitotenv.2019.02.145
20. Jia T, Wu J, Xiao Y, Liu Q, Wu Q, Qi Y, Qi X (2021) Self-grown oxygen vacancies-rich CeO_2/BiOBr Z-scheme heterojunction decorated with rGO as charge transfer channel for enhanced photocatalytic oxidation of elemental mercury. J Colloid Interface Sci 587:402–416. https://doi.org/10.1016/j.jcis.2020.12.005
21. Bijanzad K, Tadjarodi A, Akhavan O, Khiavi MM (2015) Solid state preparation and photocatalytic activity of bismuth oxybromide nanoplates. Res Chem Intermed 42:2429–2447. https://doi.org/10.1007/s11164-015-2159-2
22. Huo Y, Zhang J, Miao M, Jin Y (2012) Solvothermal synthesis of flower-like BiOBr microspheres with highly visible-light photocatalytic performances. Appl Catal B 111–112:334–341. https://doi.org/10.1016/j.apcatb.2011.10.016
23. Cao L, Ma D, Zhou Z, Xu C, Cao C, Zhao P, Huang Q (2019) Efficient photocatalytic degradation of herbicide glyphosate in water by magnetically separable and recyclable BiOBr/Fe_3O_4 nanocomposites under visible light irradiation. Chem Eng J 368:212–222. https://doi.org/10.1016/j.cej.2019.02.100
24. Jia Y, Liu P, Wang Q, Wu Y, Cao D, Qiao QA (2021) Construction of Bi_2S_3-BiOBr nanosheets on TiO_2 NTA as the effective photocatalysts: pollutant removal, photoelectric conversion and hydrogen generation. J Colloid Interface Sci 585:459–469. https://doi.org/10.1016/j.jcis.2020.10.027
25. Li Z, Ivanenko A, Meng X, Zhang Z (2019) Photocatalytic oxidation of methanol to formaldehyde on bismuth-based semiconductors. J Hazard Mater 380:120822. https://doi.org/10.1016/j.jhazmat.2019.120822
26. Tie W, Du Z, Yue H, Sarathi Bhattacharyya S, Zheng Z, He W, Hee Lee S (2020) Self-assembly of carbon nanotube/graphitic-like flake/BiOBr nanocomposite with 1D/2D/3D heterojunctions for enhanced photocatalytic activity. J Colloid Interface Sci 579:862–871. https://doi.org/10.1016/j.jcis.2020.06.088
27. Sun J, Li X, Zhao Q, Liu B (2021) Ultrathin nanoflake-assembled hierarchical BiOBr microflower with highly exposed 001 facets for efficient photocatalytic degradation of gaseous ortho-dichlorobenzene. Appl Catal B. https://doi.org/10.1016/j.apcatb.2020.119478
28. Jia X, Han Q, Liu H, Li S, Bi H (2020) A dual strategy to construct flowerlike S-scheme BiOBr/$BiOAc_1$−Br heterojunction with enhanced visible-light photocatalytic activity. Chem Eng J. https://doi.org/10.1016/j.cej.2020.125701
29. Wang Y, Wang K, Wang J, Wu X, Zhang G (2020) Sb_2WO_6/BiOBr 2D nanocomposite S-scheme photocatalyst for NO removal. J Mater Sci Technol 56:236–243. https://doi.org/10.1016/j.jmst.2020.03.039
30. Huang X, Deng Q, Liao H, Deng H, Jiang J, Zhang L, Yao X (2021) Synthesis of recyclable 3D LC/h-ZIF-8 by Zn(II) containing wastewater for photocatalytic degradation of mixed-dye under UV-Vis irradiation. J Environ Chem Eng. https://doi.org/10.1016/j.jece.2020.104978

31. Tong Y-Y, Li Y-F, Sun L, Yang R, Zhang S, Fu Y, Cao L, Chen R (2020) The prominent photocatalytic activity with the charge transfer in the organic ligand for $[Zn_4O(BDC)_3]$ MOF-5 decorated Ag_3PO_4 hybrids. Sep Purif Technol. https://doi.org/10.1016/j.seppur.2020.117142
32. Zhang X, Chen Z, Luo Y, Han X, Jiang Q, Zhou T, Yang H, Hu J (2021) Construction of NH_2-MIL-125(Ti)/CdS Z-scheme heterojunction for efficient photocatalytic H_2 evolution. J Hazard Mater 405:124128. https://doi.org/10.1016/j.jhazmat.2020.124128
33. Tu Y, Ling L, Li Q, Long X, Liu N, Li Z (2020) Greatly enhanced photocatalytic activity over Bi_2WO_6 by MIL-53(Fe) modification. Opt Mater. https://doi.org/10.1016/j.optmat.2020.110500
34. Sadeghian S, Pourfakhar H, Baghdadi M, Aminzadeh B (2021) Application of sand particles modified with NH_2-MIL-101(Fe) as an efficient visible-light photocatalyst for Cr(VI) reduction. Chemosphere 268:129365. https://doi.org/10.1016/j.chemosphere.2020.129365
35. Zhang H, Yu Z, Jiang R, Hou Y, Huang J, Zhu H, Yang F, Li M, Li F, Ran Q (2021) Metal organic frameworks constructed heterojunction with α-NiS-β-NiS/CdS: The effect of organic-ligand in UiO-66 for charge transfer of photocatalytic hydrogen evolution. Renew Energy 168:1112–1121. https://doi.org/10.1016/j.renene.2020.12.102
36. Aleksandrzak M, Sielicki K, Mijowska E (2020) Enhancement of photocatalytic hydrogen evolution with catalysts based on carbonized MOF-5 and g-C_3N_4. RSC Adv 10:4032–4039. https://doi.org/10.1039/c9ra08388j
37. Cui L, Zou X, Liu Y, Li X, Jiang L, Li C, Yang L, Yu M, Wang Y (2020) Dramatic enhancement of photocatalytic H2 evolution over hydrolyzed MOF-5 coupled $Zn_{0.2}Cd_{0.8}S$ heterojunction. J Colloid Interface Sci 577:233–241. https://doi.org/10.1016/j.jcis.2020.05.023
38. Younis SA, Serp P, Nassar HN (2020) Photocatalytic and biocidal activities of $ZnTiO_2$ oxynitride heterojunction with MOF-5 and g-C_3N_4: a case study for textile wastewater treatment under direct sunlight. J Hazard Mater. https://doi.org/10.1016/j.jhazmat.2020.124562
39. Jabbar A, Fiaz M, Rani S, Ashiq MN, Athar M (2020) Incorporation of CuO/TiO_2 nanocomposite into MOF-5 for enhanced oxygen evolution reaction (OER) and photodegradation of organic dyes. J Inorg Organomet Polym Mater 30:4043–4052. https://doi.org/10.1007/s10904-020-01550-5
40. Zhang C, Fei W, Wang H, Li N, Chen D, Xu Q, Li H, He J, Lu J (2020) p-n Heterojunction of BiOI/ZnO nanorod arrays for piezo-photocatalytic degradation of bisphenol A in water. J Hazard Mater 399:123109. https://doi.org/10.1016/j.jhazmat.2020.123109
41. Jeong YC, Seo JW, Kim JH, Nam S, Shin MC, Cho YS, Byeon JS, Park CR, Yang SJ (2019) Function-regeneration of non-porous hydrolyzed-MOF-derived materials. Nano Res 12:1921–1930. https://doi.org/10.1007/s12274-019-2459-8
42. Lin L, Huang M, Long L, Sun Z, Zheng W, Chen D (2014) Fabrication of a three-dimensional BiOBr/BiOI photocatalyst with enhanced visible light photocatalytic performance. Ceram Int 40:11493–11501. https://doi.org/10.1016/j.ceramint.2014.03.039
43. Firoozi M, Rafiee Z, Dashtian K (2020) New MOF/COF hybrid as a robust adsorbent for simultaneous removal of Auramine O and Rhodamine B dyes. ACS Omega 5:9420–9428. https://doi.org/10.1021/acsomega.0c00539
44. Yu H, Huang B, Wang H, Yuan X, Jiang L, Wu Z, Zhang J, Zeng G (2018) Facile construction of novel direct solid-state Z-scheme AgI/BiOBr photocatalysts for highly effective removal of ciprofloxacin under visible light exposure: Mineralization efficiency and mechanisms. J Colloid Interface Sci 522:82–94. https://doi.org/10.1016/j.jcis.2018.03.056
45. Cao J, Xu B, Lin H, Luo B, Chen S (2012) Chemical etching preparation of BiOI/BiOBr heterostructures with enhanced photocatalytic properties for organic dye removal. Chem Eng J 185–186:91–99. https://doi.org/10.1016/j.cej.2012.01.035
46. Yu L, Zhang X, Li G, Cao Y, Shao Y, Li D (2016) Highly efficient $Bi_2O_2CO_3$ /BiOCl photocatalyst based on heterojunction with enhanced dye-sensitization under visible light. Appl Catal B 187:301–309. https://doi.org/10.1016/j.apcatb.2016.01.045
47. Li J, Yang F, Zhou Q, Ren R, Wu L, Lv Y (2019) A regularly combined magnetic 3D hierarchical Fe_3O_4/BiOBr heterostructure: fabrication, visible-light photocatalytic activity and degradation mechanism. J Colloid Interface Sci 546:139–151. https://doi.org/10.1016/j.jcis.2019.03.028